# UC San Diego

## UC San Diego Previously Published Works

### Title

Soliton superlattices in twisted hexagonal boron nitride

### Permalink

https://escholarship.org/uc/item/3dm632rz

### Journal

Nature Communications, 10(1)

### ISSN

2041-1723

### Authors

Ni, GX
Wang, H
Jiang, B-Y
et al.

### Publication Date

2019

### DOI

10.1038/s41467-019-12327-x

Peer reviewed

eScholarship.org Powered by the California Digital Library
University of California

nature COMMUNICATIONS

ARTICLE

https://doi.org/10.1038/s41467-019-12327-x OPEN

# Soliton superlattices in twisted hexagonal boron nitride

G.X. Ni[1], H. Wang[2], B.-Y. Jiang[3], L.X. Chen[2], Y. Du[3], Z.Y. Sun[3], M.D. Goldflam[3], A.J. Frenzel[3], X.M. Xie[2], M.M. Fogler[3] & D.N. Basov[1]

Properties of atomic van der Waals heterostructures are profoundly influenced by interlayer coupling, which critically depends on stacking of the proximal layers. Rotational misalignment or lattice mismatch of the layers gives rise to a periodic modulation of the stacking, the moiré superlattice. Provided the superlattice period extends over many unit cells, the coupled layers undergo lattice relaxation, leading to the concentration of strain at line defects – solitons - separating large area commensurate domains. We visualize such long-range periodic superstructures in thin crystals of hexagonal boron nitride using atomic-force microscopy and nano-infrared spectroscopy. The solitons form sub-surface hexagonal networks with periods of a few hundred nanometers. We analyze the topography and infrared contrast of these networks to obtain spatial distribution of local strain and its effect on the infrared-active phonons of hBN.

[1] Department of Physics, Columbia University, New York, NY 10027, USA. [2] State Key Laboratory of Functional Materials for Informatics, Shanghai Institute of Microsystem and Information Technology, Chinese Academy of Sciences, 865 Changning Road, 200050 Shanghai, P. R. China. [3] Department of Physics, University of California, San Diego, La Jolla, CA 92093, USA. Correspondence and requests for materials should be addressed to D.N.B. (email: db3056@columbia.edu)

Periodic modulation of interlayer stacking in two-dimensional van der Waals (vdWs)-based systems provide a unique control of their physical properties[1–18] not available in commonplace epitaxial heterostructures. Prominent examples include twisted bilayer graphene (TBG), graphene on lattice-mismatched hBN substrate[1,3–8,10–18], and hetero-bilayers of transition metal dichalcogenides[9,19]. In particular, the moiré superlattice in TBG at the "magic" twist angle $\theta \approx 1°$ gives rise to strong electron correlations and superconductivity[2,20]. On the other hand, a network of solitons forming in TBG at smaller $\theta$[2,11,13,14,21,22], radically alters its electronic[13,21–24] and plasmonic[14,23,25] properties. Here we report on nano-imaging of soliton superlattices in hexagonal boron nitride (hBN). The solitons appear to originate at a misfit atomic plane located ~15 nm beneath the surface of hBN crystals. Utilizing scattering-type scanning near-field optical microscope (s-SNOM), we uncovered that networks of these buried soliton superlattices are registered in infrared (IR) spectral features associated with dipole-active phonons of hBN. We modeled the near-field IR contrast of the solitons in terms of local hardening and broadening of the phonon modes, which we related to the distribution of the elastic strain in the system.

## Results

**Topography of hBN domain patterns**. We begin with the topographic images of the hBN domain patterns (Fig. 1a–e) obtained with the atomic force microscope (AFM). The patterns extend over macroscopic areas (>$10^4$ μm$^2$) and have periods $\Lambda_1$, $\Lambda_2 \sim 300$–$800$ nm. The domains vary from nearly perfectly hexagonal (Fig. 1b) to highly distorted, diamond-like motifs (Fig. 1e). The domain boundaries are demarcated by the dips in the topography, which are about $w \sim 90$ nm wide (Fig. S2 of Supplementary Information). Macroscopic domain patterns are not impacted by defects on the sample surface such as wrinkles[26]: the white lines of elevated topography in Fig. 1a–d. Similarly, the domain boundaries do not disturb the 14-nm-periodic moiré pattern formed by monolayer graphene deposited on top of hBN (Fig. 1e, inset). Both observations suggest that the long-range superlattices form at some depth $d$ below the surface of the hBN crystal. Based on a theoretical model for the strain distribution around a soliton, we estimate $d \sim w/7 \sim 15$ nm (Supplementary Information Section 2).

**Origin of hBN soliton superlattices**. For an in-depth look at the solitons, we focus on two representative cases (Fig. 1b, e). The locations of the domain-wall junctions in these images, connected by straight lines, are plotted in Fig. 2c–h. These latter plots reveal somewhat deformed lattices whose primitive periods $\Lambda_1$, $\Lambda_2$ (Fig. 1c) vary in space. We can relate such variations to the interlayer strain and rotation in the system, or more precisely, to the averaged (coarse-grained) strain tensor $\bar{u}_{\alpha\beta}$ and twist angle $\bar{\theta}$. Figure 2 illustrates the calculated color maps of $\bar{u}_{\alpha\beta}(\mathbf{r})$ and $\bar{\theta}(\mathbf{r})$ superimposed on the soliton meshes. Here $\alpha, \beta \in \{x, y\}$ and $\mathbf{r} = (x, y)$ is the in-plane position. Note that the angles at all the soliton junctions are close to 120°, which is analogous to the Plateau law of foam films[27] (see Supplementary Information Section 3 for details). For domains shaped as unilateral hexagons, we find an isotropic and predominantly tensile average strain $\bar{u}_{xx}, \bar{u}_{yy} \sim 0.05\%$ with the average twist angle $\bar{\theta} \sim 10^{-4}$ rad $\approx 0.01°$. For diamond-like domains, the strain is anisotropic, almost uniaxial. A couple of remarks on these results are in order. First, the coarse-grained strain $\bar{u}_{\alpha\beta}$ should not be confused with the local strain $u_{\alpha\beta}$, which is to be discussed below. Second, the calculation of $\bar{u}_{\alpha\beta}$ and $\bar{\theta}$ requires as an input the Burgers vector $\mathbf{b}_j$ of the solitons. These vectors connect the nearest identical atoms (e.g., borons) in the same atomic plane. They have magnitude $b = 0.25$ nm each and angular directions separated by 120°. However, since our AFM does not resolve the hBN crystal orientation, we do not know these directions. To generate Fig. 2 we chose one of these directions along the $x$-axis of the plot (Fig. 2a, b). If the Burgers vectors are rotated through some common angle, qualitatively similar $\bar{u}_{\alpha\beta}(\mathbf{r})$ and $\bar{\theta}(\mathbf{r})$ maps are obtained.

**Nano-IR imaging of hBN superlattices**. We proceed to the survey of the results obtained by the IR nano-imaging. We have carried out these scanning nano-spectroscopy experiments in the frequency region of hBN phonon polaritons[28–32]. In our s-SNOM apparatus the metalized AFM tip was illuminated by IR light thus generating a strong enhancement of the electric field underneath the tip (Fig. 3a)[4,33]. Such an antenna-based nano-IR setup solves the problem of the photon-polariton momentum mismatch[33–35] and enables local spectroscopy of polariton modes in hBN with ~25 nm spatial resolution (see the "Methods" section). Employing

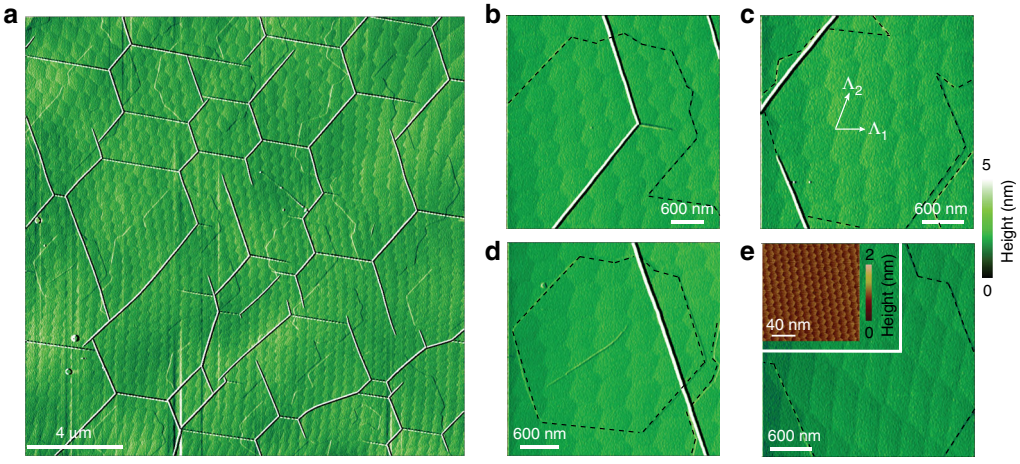


**Fig. 1** AFM topography images. **a** Large-scale image of hBN crystals showing the periodic domain pattern. **b**–**e** Zoom-in view of different smaller regions revealing varied domain shapes. The dashed black lines are the contours of graphene epitaxial grown on hBN. Inset of **e** displays a high-resolution topography (friction-AFM) image demonstrating the small-period Moiré pattern at the graphene/hBN interface. The large-period domain patterns are influenced neither by the presence of graphene nor by hBN wrinkles (the white lines in **a**–**d**) on the top surface of the crystal

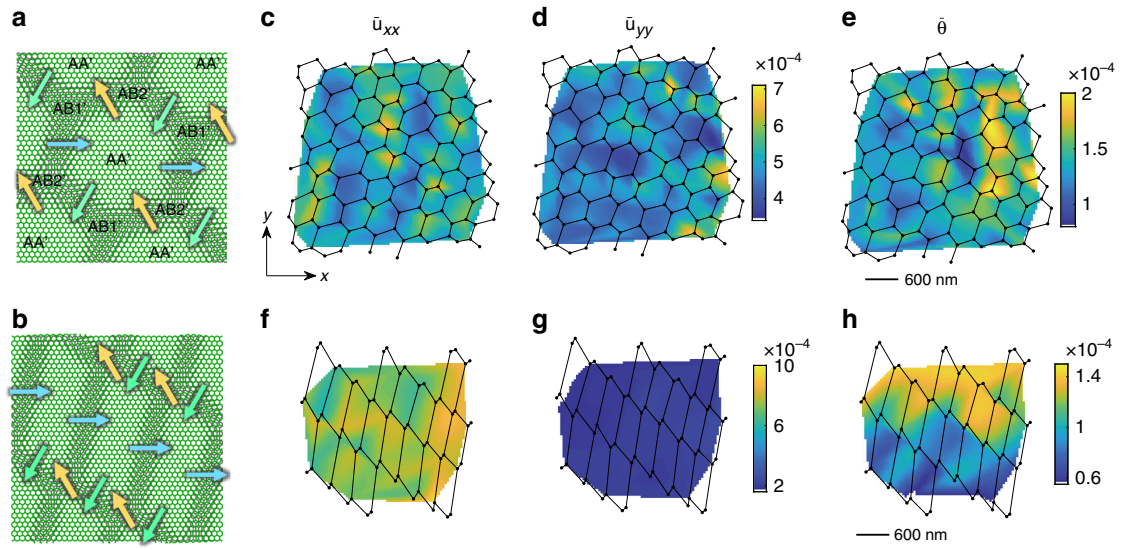


**Fig. 2 a**, **b** Schematic diagram of the soliton superlattice in hBN. The shift of the lattice sites in the two adjacent misfit atomic layers (green and gray) is concentrated at the solitons (misfit dislocations). Each soliton is characterized by one of the three possible Burgers vectors displayed with arrows. The regions of AA′, AB1′, and AB2′ stacking are labeled. **c**–**h** Solitons (lines), their junctions (dots), and the corresponding maps of coarse-grained quantities: **c**, **f** *x*-axis average tensile strain $\bar{u}_{xx}$, **d**, **g** *y*-axis average tensile strain $\bar{u}_{yy}$, **e**, **h** average rotation angle $\bar{\theta}$ (rad). The average shear strain $\bar{u}_{xy}$ is small everywhere and not shown. The top row panels **c**–**e** are deduced from Fig. 1b; the bottom row panels **f**–**h** are obtained from Fig. 1e

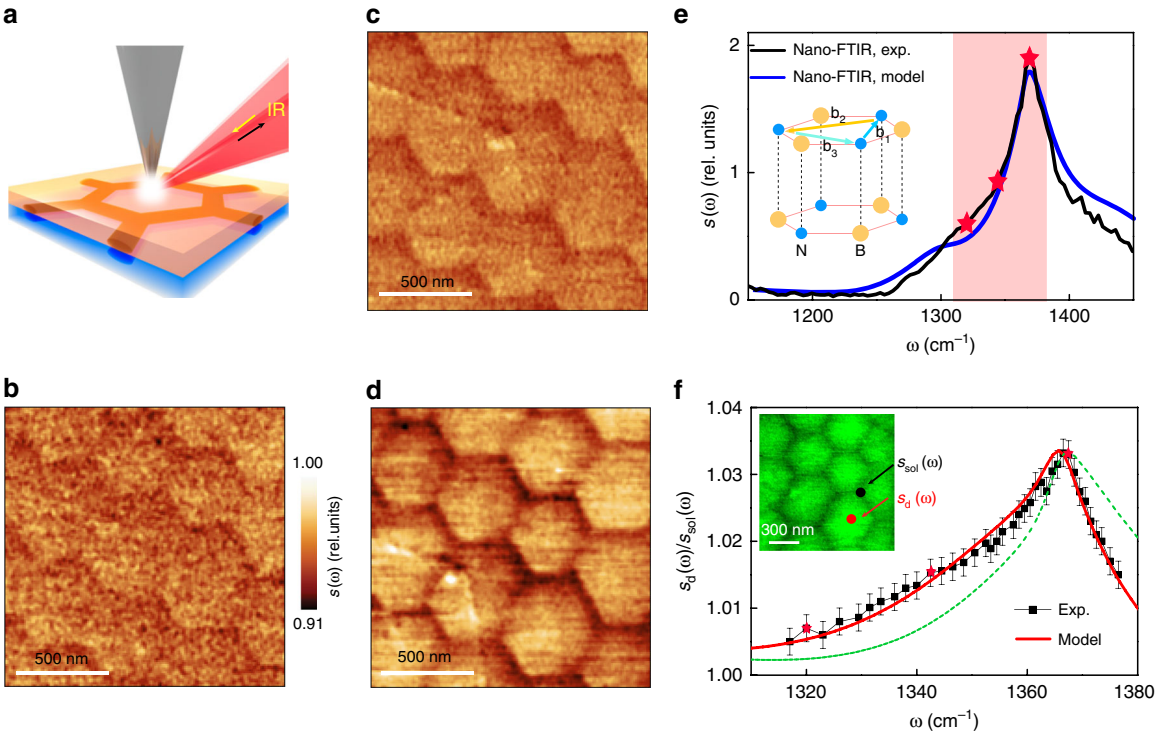


**Fig. 3** Solitons and lattice dynamics of hBN by nano-IR imaging and spectroscopy. **a** Schematic of the nano-IR imaging showing an AFM tip illuminated by a focused IR beam. The solitons reside at the atomic interface between two parts of the hBN slab (yellow and blue regions). The orange and blue cylinders delineating one hexagonal domain inside the slab represent the strain distribution around the solitons. **b**–**d** Nano-IR images of hBN domain patterns at frequencies 1320, 1344, and 1368 $cm^{-1}$, respectively. These frequencies are marked with red stars and dots in panels e and f. **e** Typical nano-FTIR spectrum of an hBN crystal. Black line: experimental data, blue spectrum: theoretical model described in the text. The inset illustrates the AA′ stacking of hBN and the three possible Burgers vectors $\mathbf{b}_j$. The shaded area highlights the spectral range analyzed in panel **f**. **f** The $s_d(\omega)/s_{sol}(\omega)$ spectra across the hBN phonon polariton band. The error bars represent the 90% confidence intervals. The red solid line is the best fit to the data (black squares) using the frequency and the damping rate of the hBN optical phonon as adjustable parameters. The green line is the best fit obtained by varying the damping rate only. The inset shows the AFM topography corresponding to the IR images in panels **b**–**d**

tunable quantum cascade lasers, we acquired nano-IR images at more than 50 different discrete frequencies. We found that the domain patterns revealed by the AFM topography are also prominent in the nano-IR images (Fig. 3b–d). We obtained nano-IR data with both monochromatic tunable quantum cascade lasers (Fig. 3b–d, f) and also broadband difference frequency generation sources (Fig. 3e) using Fourier transform spectroscopy. The strongest contrast is observed at frequency $\omega = 1368\,\mathrm{cm}^{-1}$ (Fig. 3d), which corresponds to the phonon polariton resonance of hBN (Fig. 3e). The contrast systematically weakens as $\omega$ is shifted away from $\omega = 1368\,\mathrm{cm}^{-1}$. In all the images the back-scattering amplitude $s(\omega, \mathbf{r})$ is enhanced at the centers of the domains ($s = s_\mathrm{d}(\omega)$) and reduced at the solitons ($s = s_\mathrm{sol}(\omega)$). We therefore conclude that the lattice dynamics is modified near the solitons where the strain is concentrated. The frequency dependence of the ratio $s_\mathrm{d}(\omega)/s_\mathrm{sol}(\omega)$ highlights subtle yet systematic variations of this modified lattice response. This ratio exhibits an asymmetric maximum, with a broader low-frequency side (Fig. 3f).

**Elucidating nano-IR response**. Quantitative modeling of the nano-IR response is a challenging task that goes beyond the scope of the present work. To analyze the $s_\mathrm{d}(\omega)/s_\mathrm{sol}(\omega)$ spectra, we restricted ourselves to the simplified approach, similar those in recent nano-IR study of wrinkled and strained hBN crystals[26] and an earlier work on nano-indented SiC[36]. We assumed that the hBN crystal can be described by a permittivity tensor $\varepsilon_\alpha(\omega, \mathbf{r})$ varying only as a function of *in-plane* coordinates. Here $\alpha = \perp(||)$ is the in-plane (out-of-the-plane) component. We further assumed that the near-field amplitude $s(\omega, \mathbf{r})$ depends only on the local value of $\varepsilon_\alpha(\omega, \mathbf{r})$. We adopted the standard Lorentzian model for the hBN permittivity,

$$\frac{\varepsilon_\alpha(\omega)}{\varepsilon_{\infty,\alpha}} = 1 + \frac{\omega_{\mathrm{LO},\alpha}^2 - \omega_{\mathrm{TO},\alpha}^2}{\omega_{\mathrm{TO},\alpha}^2 - \omega^2 - i\omega\Gamma_\alpha}, \qquad (1)$$

where $\omega_{\mathrm{TO},\alpha}$ ($\omega_{\mathrm{LO},\alpha}$) is the transverse (longitudinal) optical phonon frequency and $\Gamma_\alpha$ is the broadening[35], which we treated as adjustable parameters. We numerically simulated the near-field scattering amplitude $s(\omega)$ modeling the tip as an elongated conducting spheroid and taking into account the presence of the quartz substrate underneath hBN[10]. Through these simulations we found that the nano-IR contrast can be attributed to the broadening of the phonon resonance, from $\Gamma_\perp = 6.5\,\mathrm{cm}^{-1}$ at the domain centers to $7.35\,\mathrm{cm}^{-1}$ at the walls. The dashed green trace in Fig. 3f illustrates the effect of this extra broadening alone. In addition, a minute blue shift of $\omega_{\mathrm{TO},\perp}$ from 1365.5 to $1365.8\,\mathrm{cm}^{-1}$ helps to better account for the spectral form of $s_\mathrm{d}(\omega)/s_\mathrm{sol}(\omega)$, as shown by the red line in Fig. 3f (for more details of these fits, see Supplementary Information Section 4).

Our analysis of the nano-IR line-form in Fig. 3 is phenomenological. The microscopic approach can be developed by relating the phonon frequency shift $\Delta\omega_{\mathrm{TO},\perp}$ to the local strain. Notably, the frequency shift caused by the strain is not a single number. As shown by recent first-principles calculations[26], a uniaxial strain splits the degenerate TO mode of hBN into two separate modes of orthogonal in-plane polarization. Moreover, from symmetry consideration we can predict that for an arbitrary strain, the fractional frequency shifts of these two modes should be:

$$\frac{\Delta\omega_{\mathrm{TO},\perp}}{\omega_{\mathrm{TO},\perp}} = -\frac{A+B}{2}\left(u_{xx}+u_{yy}\right) \pm \sqrt{\left[\frac{A-B}{2}\left(u_{xx}-u_{yy}\right)\right]^2 + \left(Cu_{xy}\right)^2} \qquad (2)$$

where $A$, $B$, $C \sim 1$are constants (Supplementary Information Section 5). Effectively, the strain turns hBN from the uniaxial hyperbolic material into a bi-axial one, analogous to molybdenum trioxide[37,38]. Because of different polarization, the two modes have different coupling to the in-plane field, which complicates the modeling. Even more arduous task is to take into account the realistic three-dimensional strain distribution around the solitons. The dependence of the strain on the in-plane coordinates is relatively weak because the characteristic width $w \sim 90$ nm of the strained region near the surface is large (Figs. 1 and S2). Nevertheless, the dependence of the strain on the depth $z$ is strong because of the anisotropic character of the strain (Fig. 3a and Supplementary Information Section 2). Leaving a quantitative study for future work, we limit ourselves to the following estimate. Qualitatively, the nano-IR amplitude measured above the soliton can be viewed as the sum of signals from all the underlying hBN layers, each with a shifted (and split) $\omega_{\mathrm{TO},\perp}$. Assuming the characteristic strain variation of $\delta u \sim b/w \sim 0.3\%$, the nano-IR line-shape is expected to acquire an additional inhomogeneous broadening $\Delta\Gamma_\perp \sim \omega_{\mathrm{TO},\perp}\delta u \sim 4\mathrm{cm}^{-1}$. This estimate is of the same order of magnitude as the fit parameter quoted above.

## Discussion

The confinement of both the topographic and nano-IR contrast to narrow regions along the domain walls is consistent with the notion that the individual layers in hBN are not rigid but instead behave as deformable atomic membranes prone to incommensurate–commensurate transitions. The key signature of these transitions is the formation of structural solitons where mechanical strain is accumulated[11–15]. Previously, the transmission electron microscopy and second harmonic generation experiments have identified isolated solitons[39] in few-layer-thin hBN specimens. Our work demonstrates that the solitons can form in the interior of a bulk vdW crystal, not just at the surface or in few-layer systems, and that they can organize themselves in large regular superlattices. We have also demonstrated that nano-IR imaging can be applied to map the local strain field in a polar crystal[26,36].

The observed residual strain concentrated in the solitons, could originate from multiple sources, one of which is the difference in the thermal expansion coefficients of hBN and graphene deposited on top of it ($-8\times10^{-6}$/K for graphene[40] and $-3\times10^{-6}$/K for hBN[41]). A rough estimate of the lattice mismatch that could develop during the cooling of the sample is $[(-8)-(-3)]\times10^{-6}$/K×(1150–20) K = 0.6%, which is close to the critical mismatch for the commensurate–incommensurate transition in an hBN bilayer[42].

Finally, we mention several predictions testable by atomic-resolution or stacking-sensitive probes. Unlike TBG, where the lowest-energy stacking is AB stacking and the domains are triangular[1,6,14,18], the hexagonal domains in hBN are of AA′ type (Figs. 2a and 3e), the lowest-energy stacking in hBN[43]. For the domain-wall junctions in hBN, we expect two distinct stacking types, AB1′ and AB2′, that alternate in space (Fig. 2a). Future studies may also seek to observe changes in the electronic structure in hBN moiré superlattices[44]. More broadly, it will be fruitful to explore *in operando* tuning of the twist angle[45] and attendant lattice, electronic[2,46], plasmonic[15] and possibly excitonic[8,9] responses of various vdW materials.

## Methods

**Sample synthesis**. The hBN flakes were prepared on quartz substrates using mechanical exfoliation. hBN/Quartz samples were then transferred into chemical vapor deposition chamber and annealed at 1150 °C at low pressure with continuous argon flow of 50 standard cubic centimeters per minute (s.c.c.m.) for 30 min. After that, $CH_4$:$H_2$ at 5:5 s.c.c.m. were injected into the chamber for 300 min at pressures below 12 mbar—a process used for graphene growth[39]. Finally, samples are cooled to room temperature in argon flow.

**Nano-IR imaging**. The IR nano-imaging experiments were performed using s-SNOM (neaspec.com) equipped with continuous wave mid-IR quantum cascade lasers (daylightsolutions.com). The s-SNOM is based on AFM with curvature radius ~ 25 nm operating in the tapping mode with a tapping frequency around 270 kHz. A pseudo-heterodyne interferometric detection module was implemented to extract both the scattering amplitude *s* and the phase of the near-field signal. In the current work, we discuss the amplitude of the signal. In order to subtract the background signal, we demodulated the near-field signal at the third harmonics of the tapping frequency. All the IR nano-imaging experiments were performed in ambient conditions. We used quantum cascade lasers with tunable frequency and a broad-band difference frequency generation laser systems.

## Data availability

The data supporting the findings of this work are available from the corresponding author upon reasonable request.

Received: 30 April 2019 Accepted: 22 August 2019
Published online: 25 September 2019

## References

1. Bistritzer, R. & MacDonald, A. H. Moiré bands in twisted double-layer graphene. *Proc. Natl Acad. Sci. USA* **108**, 12233–12237 (2011).
2. Cao, Y. et al. Unconventional superconductivity in magic-angle graphene superlattices. *Nature* **556**, 43–50 (2018).
3. Geim, A. K. & Grigorieva, I. V. Van der Waals heterostructures. *Nature* **499**, 419–425 (2013).
4. Basov, D. N., Fogler, M. M. & Garcia de Abajo, F. J. Polaritons in van der Waals materials. *Science* **354**, aag1992 (2016).
5. Low, T. et al. Polaritons in layered two-dimensional materials. *Nat. Matters* **16**, 182–194 (2017).
6. Yoo, H. et al. Atomic reconstruction at van der Waals interface in twisted bilayer graphene. arXiv:1804.03806 (2018).
7. Fang, H. et al. Strong interlayer coupling in van der Waals heterostructures built from single-layer chalcogenides. *Proc. Natl Acad. Sci. USA* **111**, 6198–6202 (2014).
8. Yu, H., Liu, G. B., Tang, J., Xu, X. & Yao, W. Moiré excitons: from programmable quantum emitter arrays to spin–orbit-coupled artificial lattices. *Sci. Adv.* **3**, e1701696 (2017).
9. Wu, F., Lovorn, T. & MacDonald, A. H. Topological exciton bands in moiré heterojunctions. *Phys. Rev. Lett.* **118**, 147401 (2017).
10. Song, J. C. W., Shytov, A. V. & Levitov, L. S. Electron interactions and gap opening in graphene superlattices. *Phys. Rev. Lett.* **111**, 266801 (2013).
11. Alden, S. J. et al. Strain solitons and topological defects in bilayer graphene. *Proc. Natl Acad. Sci. USA* **110**, 11256–11260 (2013).
12. Woods, C. R. et al. Commensurate–incommensurate transition for graphene on hexagonal boron nitride. *Nat. Phys.* **9**, 329–340 (2013).
13. San-Jose, P. & Prada, E. Helical networks in twisted bilayer graphene under interlayer bias. *Phys. Rev. B* **88**, 121408(R) (2013).
14. Sunku, S. S. et al. Photonic crystals for nano-light in moiré graphene superlattices. *Science* **362**, 1153–1156 (2018).
15. Ni, G. X. et al. Plasmons in graphene moiré superlattices. *Nat. Matters* **14**, 1217–1222 (2015).
16. Shi, Z. et al. Gate-dependent pseudospin mixing in graphene/Boron nitride moiré superlattices. *Nat. Phys.* **10**, 743–747 (2014).
17. Yankowitz, M., Ma, Q., Jarillo-Herrero, P. & LeRoy, B. J. van der Waals heterostructures combining graphene and hexagonal boron nitride. *Nat. Rev. Phys.* **1**, 112–125 (2019).
18. Tomadin, A., Polini, M. & Jung, J. Plasmons in realistic graphene/hexagonal boron nitride moiré patterns. *Phys. Rev. B* **99**, 035432 (2019).
19. Schaibley, J. R. et al. Valleytronics in 2D materials. *Nat. Rev. Mater.* **1**, 16055 (2016).
20. Yankowitz, M. et al. Tuning superconductivity in twisted bilayer graphene. *Science* https://doi.org/10.1126/science.aav1910 (2019).
21. Huang, S. et al. Topologically protected helical states in minimally twisted bilayer graphene. *Phys. Rev. Lett.* **121**, 037702 (2018).
22. Kim, K. et al. Tunable moiré bands and strong correlations in small-twist-angle bilayer graphene. *Proc. Natl Acad. Sci. USA* **114**, 3364–3369 (2017).
23. Jiang, B.-Y. et al. Plasmon reflections by topological electronic boundaries in bilayer graphene. *Nano. Lett.* **17**, 7080 (2017).
24. Ju, L. et al. Topological valley transport at bilayer graphene domain walls. *Nature* **520**, 650 (2015).
25. Jiang, L. et al. Soliton-dependent plasmon reflection at bilayer graphene domain walls. *Nat. Mater.* **15**, 840–844 (2016).
26. Lyu, B. et al. Phonon polariton-assisted infrared nanoimaging of local strain in hexagonal boron nitride. *Nano Lett.* **19**, 1982–1989 (2019).
27. Atkin, J. M., Berweger, S., Jones, A. C. & Raschke, M. B. Nano-optical imaging and spectroscopy of order, phases, and domains in complex solids. *Adv. Phys.* **61**, 745–842 (2012).
28. Caldwell, J. D. et al. Atomic-scale photonic hybrids for mid-infrared and terahertz nanophotonics. *Nat. Nano* **11**, 9–15 (2016).
29. Dai, S. et al. Tunable phonon polaritons in atomically thin van der Waals crystals of boron nitride. *Science* **343**, 1125 (2014).
30. Caldwell, J. D. et al. Photonics with hexagonal boron nitride. *Nat. Rev. Mater.* **4**, 552–567 (2019).
31. Ambrosio, A. et al. Selective excitation and imaging of ultraslow phonon polaritons in thin hexagonal boron nitride crystals. *Light.: Sci. Appl.* **7**, 27 (2018).
32. Li, P. et al. Hyperbolic phonon-polaritons in boron nitride for near-field optical imaging and focusing. *Nature Comm.* **6**, 7507 (2015).
33. Fei, Z. et al. Gate-tuning of graphene plasmons revealed by infrared nano-imaging. *Nano Lett.* **11**, 4701–4705 (2011).
34. Ni, G. X. et al. Ultrafast optical switching of infrared plasmon polaritons in high-mobility graphene. *Nat. Photon.* **10**, 244–247 (2016).
35. Ni, G. X. et al. Fundamental limits to graphene plasmonics. *Nature* **557**, 530–533 (2018).
36. Huber, A. J., Ziegler, A., Köck, T. & Hillenbrand, R. Infrared nanoscopy of strained semiconductors. *Nat. Nano* **4**, 153–157 (2009).
37. Ma, W. et al. In-plane anisotropic and ultra-low-loss polaritons in a natural van der Waals crystal. *Nature* **562**, 557–562 (2018).
38. Zheng, Z. et al. A mid-infrared biaxial hyperbolic van der Waals crystal. *Sci. Adv.* **5**, 5 (2019).
39. Kim, C.-J. et al. Stacking order dependent second harmonic generation and topological defects in h-BN bilayers. *Nano Lett.* **13**, 5660–5665 (2013).
40. Yoon, D., Son, Y. W. & Cheong, H. Negative thermal expansion coefficient of graphene measured by Raman spectroscopy. *Nano Lett.* **11**, 3227 (2011).
41. Paszkowicz, W., Pelka, J. B., Knapp, M., Szyszko, T. & Podsiadlo, S. Lattice parameters and anistropic thermal expansion of the hexagonal boron nitride in the 10–297.5 K temperature range. *Appl. Phys. A* **75**, 431 (2002).
42. Lebedeva, I. V., Lebedev, A. V., Popov, A. M. & Knizhnik, A. A. Dislocations in stacking and commensurate-incommensurate phase transition in bilayer graphene and hexagonal boron nitride. *Phys. Rev. B* **93**, 235414 (2016).
43. Xian, L., Kennes, D. M., Tancogne-Dejean, N., Altarelli, M. & Rubio, A. Multi-flat bands and strong correlations in twisted bilayer boron nitride. arXiv: 1812.08097 (2018).
44. Ribeiro-Palau, R. et al. Twistable electronics with dynamically rotable heterostructures. *Science* **361**, 690–693 (2018).
45. Yankowitz, M., Xue, J. & LeRoy, B. J. Graphene on hexagonal boron nitride. *J. Phys. Condens. Matter* **26**, 303201 (2014).
46. Weaire, D. & Hutzler, S. *The Physics of Foams*. (Oxford University Press, Oxford, 1999).

## Acknowledgements

Authors acknowledge discussions with J.S. Wu, A.S. McLeod, S. Sunku, and Y.Q. Cai. Work at Columbia is supported as part of Programmable Quantum Materials, an Energy Frontier Research Center funded by the U.S. Department of Energy (DOE), Office of Science, Basic Energy Sciences (BES), under award DE-SC0019443. Work at UCSD is supported by ONR-N000014-18-1-2722. The development of mid-infrared polaritonic structures is supported by AFOSR: FA9550-15-1-0478. D.N.B. is supported by the Gordon and Betty Moore Foundation's EPiQS Initiative through Grant GBMF4533.

## Author contributions

G.X.N. performed the nanoscale infrared measurements and characterizations. B.-Y.J., Y.D., Z.Y.S. and M.M.F. provided theoretical calculations. H.W., L.X.C., and X.M.X. created the device structures. M.D.G. and A.J.F. helped with measurements. D.N.B. supervised the project. G.X.N., M.M.F., and D.N.B. co-wrote the manuscript with input from all co-authors.

## Additional information

**Supplementary Information** accompanies this paper at https://doi.org/10.1038/s41467-019-12327-x.

**Competing interests:** The authors declare no competing interests.

**Reprints and permission** information is available online at http://npg.nature.com/reprintsandpermissions/

**Peer review information** *Nature Communications* thanks the anonymous reviewers for their contribution to the peer review of this work

**Publisher's note** Springer Nature remains neutral with regard to jurisdictional claims in published maps and institutional affiliations.

**Open Access** This article is licensed under a Creative Commons Attribution 4.0 International License, which permits use, sharing, adaptation, distribution and reproduction in any medium or format, as long as you give appropriate credit to the original author(s) and the source, provide a link to the Creative Commons license, and indicate if changes were made. The images or other third party material in this article are included in the article's Creative Commons license, unless indicated otherwise in a credit line to the material. If material is not included in the article's Creative Commons license and your intended use is not permitted by statutory regulation or exceeds the permitted use, you will need to obtain permission directly from the copyright holder. To view a copy of this license, visit http://creativecommons.org/licenses/by/4.0/.

© The Author(s) 2019

Supplementary Information

# Soliton superlattices in Twisted Hexagonal Boron Nitride

G. X. Ni et al.

## 1. Raman spectroscopy

In SFig. 1, we plot a typical Raman spectrum for our hBN specimens. The full width at half maximum (FWHM) of the in-plane ($E_{2g}$) phonon mode is 8.5 $cm^{-1}$, attesting to the high quality of our samples. Note that this FWHM presumably includes some inhomogeneous broadening due to the soliton network, similar to the TO ($E_{2u}$) phonon mode we studied by the s-SNOM.

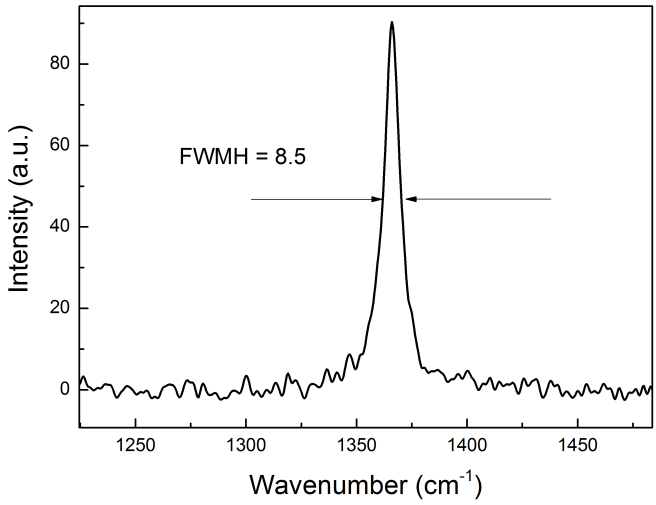


**Supplementary Figure 1 | Raman spectrum of the hBN crystal.**

## 2. Local strain and the dislocation depth estimate

Misfit dislocation networks have been studied extensively. Hexagonal networks resembling those that we observed in hBN generically appear at twist grain boundaries [S1]; References [S2, S3, S4] offer examples of experimental images for various materials. Such networks are also common in epitaxial films [S5, S6]. If the network period is large, the dislocations are far apart, and so in the first approximation we can consider each of them separately. The analysis is greatly simplified by the fact that hBN belongs to the class of hexagonal crystals, for which exact solutions for the strain distribution around single dislocations are available. Consider the case of a screw dislocation, which corresponds to a "shear" soliton [S7]. (For edge or mixed-type dislocations, the equations are more involved.) In an infinite crystal, a screw dislocation positioned on the $y$-axis produces the in-plane strain [S1]

$$u_{xy}^{\infty}(x,z) = \frac{b}{4\pi}\frac{\xi z}{x^2+\xi^2 z^2}\,, \qquad \xi = \sqrt{C_{66}/C_{44}}\,. \tag{S1}$$

Equation S1 implies that the strain is concentrated in two regions shaped as elliptic cylinders, which are located above and below the dislocation line (Fig. 3a of the main text). We find the anisotropy parameter $\xi \sim 7$ using the hBN elastic constants $C_{66} = (C_{11} - C_{12})/2 = 320$ GPa and $C_{44} \sim 7$ GPa from the literature [S8, S9]. Since $\xi \gg 1$, the strain has a much wider spread along $x$ (in-plane) than along $z$ (out-of-plane). This is a consequence of the weak interlayer coupling in hBN. In a crystal of finite thickness, the strain produced by a dislocation buried at depth $d$ below the top surface ($z = 0$), can be found using the method of images, $u_{xy}(x,z) = u_{xy}^{\infty}(x, z+d) + u_{xy}^{\infty}(x, z-d) + \cdots$. Here we showed explicitly only the two terms that dominate the strain distribution near the top surface. The characteristic width $w$ of the strained region at the surface is $w = \xi d$. Assuming it corresponds to the width $\sim 90$ nm of the minima seen in the AFM topography (SFig. 2, SFig. 3 & SFig. 4), we get the estimate of the dislocations depth $d = w/\xi \sim 15$ nm given in the main text. A more refined modeling of the strain (including buckling effects [S12, S13]) is a challenging task we leave for future work.

We observed different superlattice patterns in a large variety of hBN microcrystals (at least dozen). Therefore, the effects reported in our work are highly reproducible. In SFig. 2, 3&4 we display additional representative examples of both AFM topography and nano-IR images obtained at different frequencies. The relatively large height variations in SFig. 3 could originate from several factors (Refs. [S10, S11]). For example, collective multilayer effects, such as buckling are known to produce large high variations (Refs. [S12, S13]). It is also possible that the AFM does not measure the true height because the deformable nature of thin hBN flakes. However, we would like to emphasize that the height determination in SFig. 3 does not enter into inferences of our strain map studies. In our strain analysis, we focused on the planar distortions, which captures the key experimental results. Hence, given the imperfections of the height determination, our conclusions are still valid.

We also observed of wrinkles and folds in hBN microcrystals. Wrinkling and folding structures are a product of a high temperature (>1000 ºC) annealing process. The wrinkles are likely to form due to the mismatch of the thermal expansion coefficient between the hBN (-3 x $10^{-6}$ /K) and the underlying quartz substrate (5.5 x $10^{-7}$ /K). Consequently, a local strain would be expected near the wrinkling structures in hBN [ref. 37].

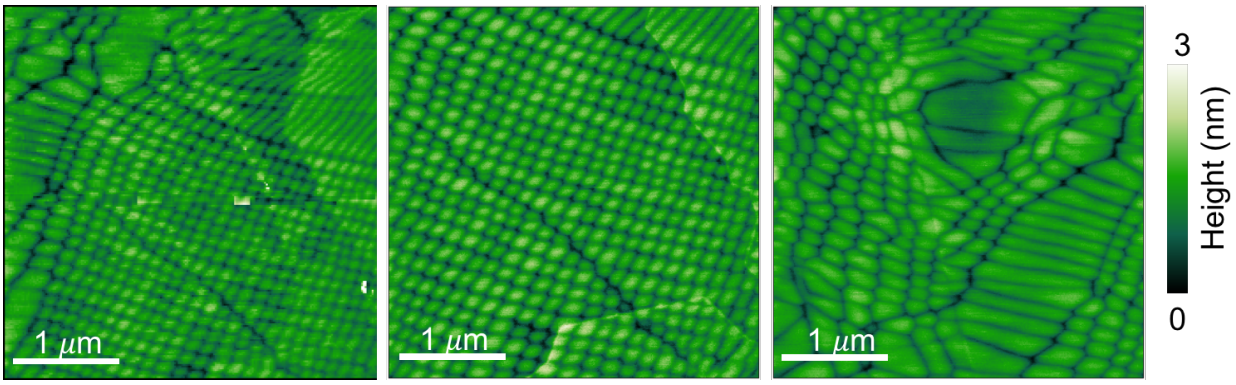

**Supplementary Figure 2 | AFM topography images of hBN crystals with different pattern structures.**

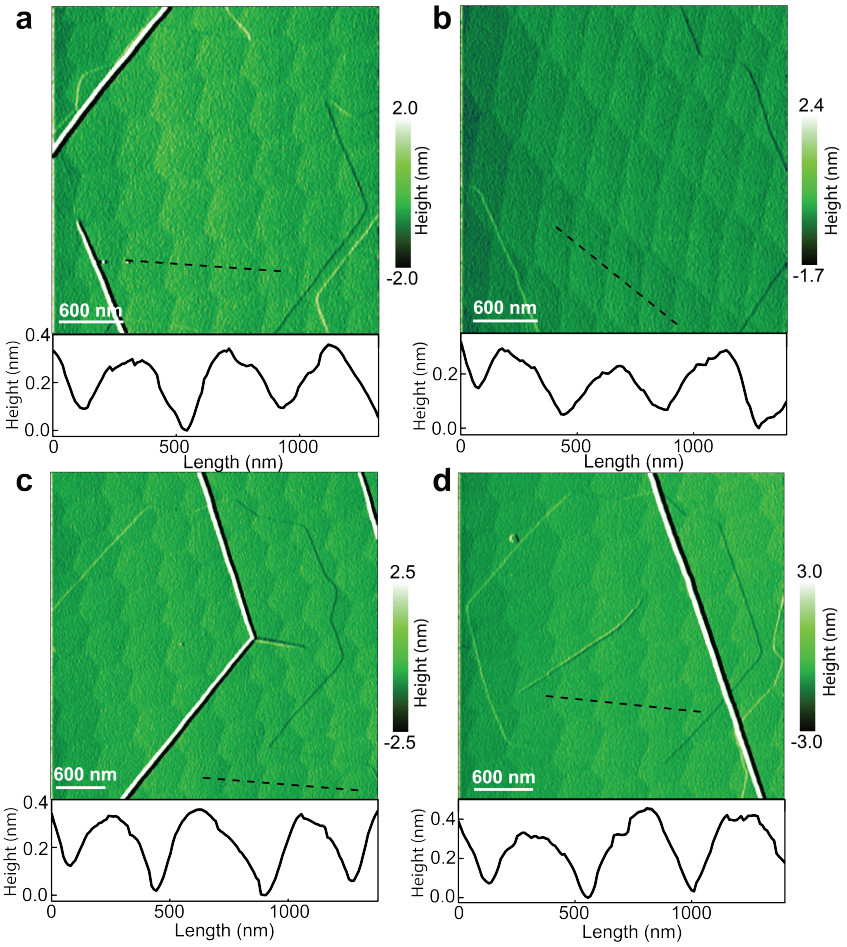


**Supplementary Figure 3 | AFM topography profiles.** Panels **a-d** are topography images and the corresponding line-cuts across the images shown in, respectively.

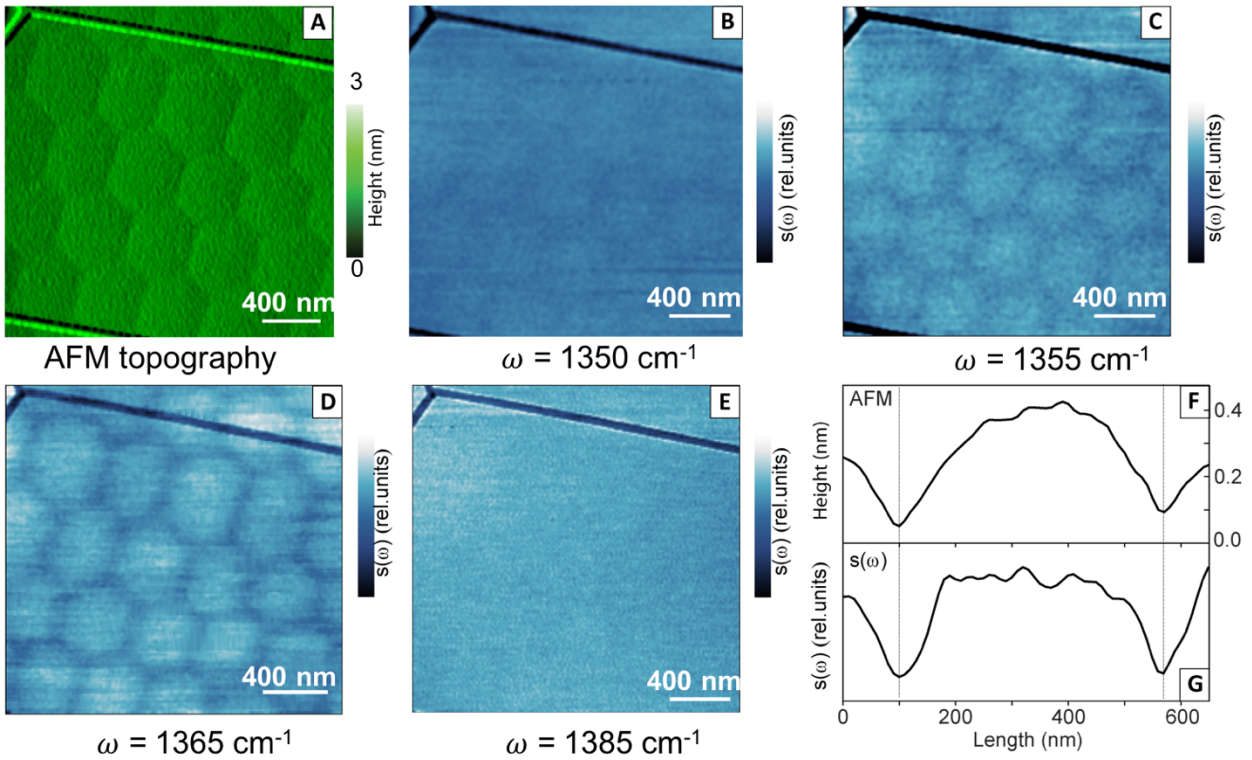


**Supplementary Figure 4 | Representative nano-IR images of soliton superlattices in hBN.** Panel A: Topography image. Panel B-E: nano-IR images at selected frequencies. These images were taken at the same as area as Panel A. Panel F: Topography line-profile across a moiré unit cell; Panel G: Phonon contrast across the same moiré unit cell as Panel F.

### 3. Coarse-grained strain and the Plateau law of dislocation networks

The coarse-grained in-plane strain tensor $\bar{u}_{\alpha\beta}$ and the twist angle $\bar{\theta}$ of the domain pattern (Fig. 2 of the main text) have been calculated according to the formulas

$$\bar{u}_{\alpha\beta} = \frac{1}{4\pi}\sum_{j=1}^{2} b_{j,\alpha}G_{j,\beta} + b_{j,\beta}G_{j,\alpha}\,, \qquad \bar{\theta} = \frac{1}{4\pi}\sum_{j=1}^{2}\left(\mathbf{G}_j \times \mathbf{b}_j\right)_z\,, \tag{S2}$$

where $\mathbf{G}_j$ is the reciprocal vector conjugate to the real-space period $\mathbf{\Lambda}_j$. These equations have been derived by noticing that whenever the observation point is shifted by either of the two primitive periods, $\mathbf{r} \to \mathbf{r} + \mathbf{\Lambda}_j$, the interlayer displacement gets incremented by the Burgers vector $\mathbf{b}_j$ of a corresponding soliton (SFig. 5a). Given the domain shape, domain size, and the orientation of the crystal lattice that defines the directions of the Burgers vectors $\mathbf{b}_j$, the calculation of $\bar{u}_{\alpha\beta}$ and $\bar{\theta}$ is straightforward. Conversely, explaining why the observed domains have such shapes and sizes presents a theoretical problem. Below we show that the location of the soliton junction $\mathbf{R}$ within the unit cell of the network is fixed by the simple rule: the arms of each junction are separated by $120°$ angles. This rule resembles the Plateau law (PL) obeyed by

foam films [S14]. Note that due to the simple parallelogram geometry of the unit cell, this position $\mathbf{R}_{\mathrm{PL}}$ is unique and independent of the Burgers vectors $\mathbf{b}_j$ unknown in our experiment.

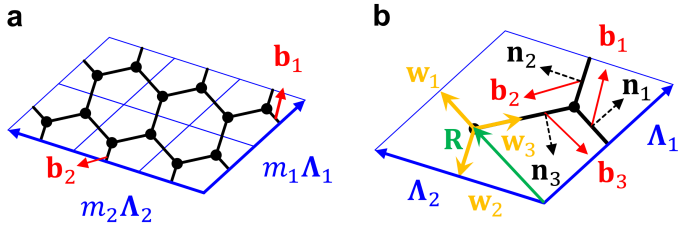


**Supplementary Figure 5 | Vectors determining the domain shape** (a) Domain wall configuration over many unit cells. (b) Within a unit cell, the domain wall directions $\mathbf{w}_j$ are characterized by the Burgers vectors $\mathbf{b}_j$, the normal vectors $\mathbf{n}_j$, and the location $\mathbf{R}$ of the domain-wall junction.

The PL can be derived as follows. The coarse-grained strain that causes the formation of the network originates from a misfit atomic plane boundary in the crystal. This misfit can be considered an external strain imposed on the system. We define the corresponding external stress $\sigma_{\alpha\beta} = C_{\alpha\beta\gamma\delta}\bar{u}_{\gamma\delta}$ where $C_{\alpha\beta\gamma\delta}$ is the (in-plane part) of the elastic constants tensor. If the system is in equilibrium, the size and shape of the solitons must provide the lowest total energy of the system under such stress. Neglecting the soliton-soliton interactions and the curvature of the soliton lines, the energy of each soliton has two parts. One part is the self-energy $E_{\mathrm{sol}} = \gamma(\phi)|\mathbf{w}|$, where $|\mathbf{w}|$ is the length of the soliton and $\gamma$ is the line tension, i.e., the soliton energy per unit length. The latter in general depends on the angle $\phi$ between the Burgers vector $\mathbf{b}$ and the normal vector $\mathbf{n} = \hat{\mathbf{w}}\times\hat{\mathbf{z}}$ of the wall. The other part of the energy,

$$E_{\mathrm{ext}} = -|\mathbf{w}|\sigma_{\alpha\beta}b_\alpha n_\beta = -\sigma_{\alpha\beta}b_\alpha(\mathbf{w}\times\hat{\mathbf{z}})_\beta\,, \tag{S3}$$

represents coupling of the soliton to the external stress. To find the position $\mathbf{R}$ of the junction, we need to minimize the total energy per unit cell,

$$E_{\mathrm{tot}} = 2\sum_{j=1}^{3}(E_{\mathrm{sol}}+E_{\mathrm{ext}})\,, \tag{S4}$$

where the factor of two appears because there are two junctions in each cell. A virtual displacement of $\mathbf{R}$ by $\Delta\mathbf{R}$ modifies all three $\mathbf{w}_j$'s by the same amount $\Delta\mathbf{w} = -\Delta\mathbf{R}$. The corresponding change to $E_{\mathrm{ext}}$ vanishes,

$$\Delta E_{\mathrm{ext}} = (\Delta\mathbf{R}\times\hat{\mathbf{z}})_\beta\sigma_{\alpha\beta}\sum_j b_{j,\alpha} = 0, \tag{S5}$$

because the Burgers vectors $\mathbf{b}_j$ add up to zero. This means that the "external energy" is independent of $\mathbf{R}$. We only need to minimize the soliton self-energy. Taking the derivative of the self-energy with respect to $\mathbf{R}$, we get, after some algebra, Eq. (19-2) of [S1]:

$$\sum_j \left[\gamma(\phi_j)\hat{\mathbf{w}}_j + (\hat{\mathbf{z}}\times\hat{\mathbf{w}}_j)\gamma'(\phi_j)\right] = 0\,. \tag{S6}$$

For the special case $\mathbf{R} = \mathbf{R}_{\mathrm{PL}}$ where the three solitons are oriented $120°$ apart, all three $\phi_j$'s are equal since $\mathbf{b}_j$'s are also oriented $120°$ apart. Additionally, $\sum_j \hat{\mathbf{w}}_j = 0$, and so Eq. (S6) is satisfied. Hence, $\mathbf{R}_{\mathrm{PL}}$ is the extremum of the self-energy. We verified numerically that this extremum is indeed the global minimum. This establishes the PL. In foams [S14], the PL follows immediately from Eq. (S6) because the surface tension $\gamma$ is a constant. In our system, $\gamma$ depends on the soliton direction. However, the PL is saved by the three-fold rotational symmetry of the hBN atomic plane. Note that the AFM images shown in Fig. 2c-e & f-h of the main text indicate some deviations from the PL, which may be because of the approximations made in the model or because of dislocation pinning by residual defects, which prevents the system from reaching full equilibrium.

### 4. Fitting of the nano-IR contrast

To simulate $s_{\mathrm{d}}(\omega)/s_{\mathrm{sol}}(\omega)$ spectra, we employed the electromagnetic solver developed previously [S15, S16]. It requires as an input the infrared reflectivity of the sample, which we calculated by accounting all the layers (air/hBN/quartz) present in the system. For hBN we used the Lorentzian permittivity model, Eq. (1) of the main text. SFigure 6 shows the calculated $s_{\mathrm{d}}(\omega)/s_{\mathrm{sol}}(\omega)$ spectra for different choices of two adjustable parameters: the damping $\Gamma_\perp$ and the optical phonon frequency $\omega_{\mathrm{TO},\perp}$. Specifically, the $s_{\mathrm{d}}(\omega)$ spectra can be fitted with the parameters $\omega_{\mathrm{TO},\perp} = 1365.5\ \mathrm{cm}^{-1}$ and $\Gamma_\perp = 6.5\ \mathrm{cm}^{-1}$, which is consistent with previous work [S17, S18, S19]. The best fit to the $s_{\mathrm{sol}}(\omega)$ spectra is obtained with $\omega_{\mathrm{TO},\perp} = 1365.8\ \mathrm{cm}^{-1}$ and $\Gamma_\perp = 7.35\ \mathrm{cm}^{-1}$.

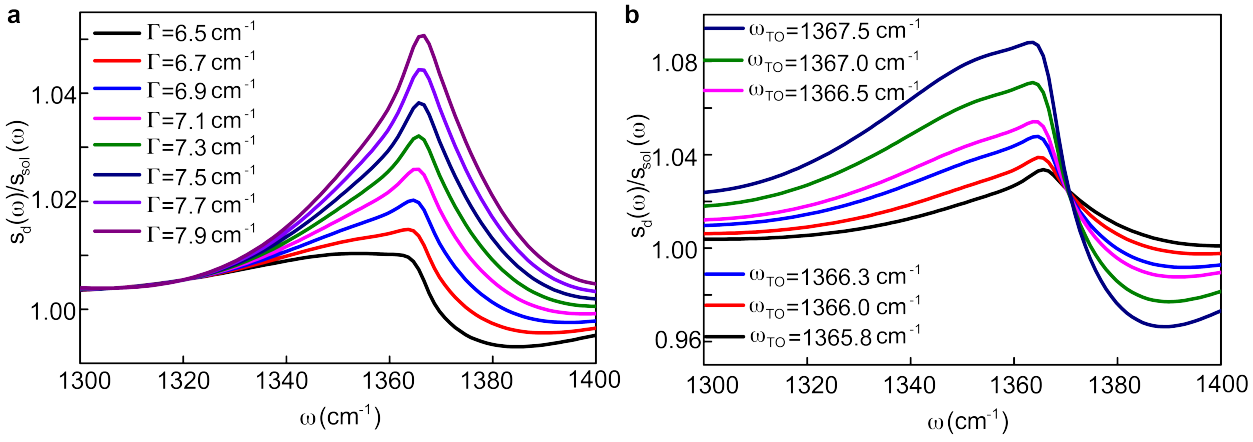


**Supplementary Figure 6 | $s_{\mathrm{d}}(\omega)/s_{\mathrm{sol}}(\omega)$ spectra fitting.** a: $s_{\mathrm{d}}(\omega)/s_{\mathrm{sol}}(\omega)$ spectra at different $\Gamma_\perp$. b: $s_{\mathrm{d}}(\omega)/s_{\mathrm{sol}}(\omega)$ spectra at different $\omega_{\mathrm{TO},\perp}$.

### 5. Phonon frequency shift due to strain

The frequencies of the two-fold degenerate $E_{2u}$ phonon mode are the eigenvalues of a certain

$2\times2$ dynamical matrix $D_{\alpha\beta}$. The perturbative effect of a weak strain on this matrix is described by the second-order elastic tensor $G_{\alpha\beta\gamma\delta}$. If we restrict attention to the in-plane coordinates, the hexagonal symmetry of the hBN planes implies that this fourth-rank tensor has only three linearly independent nonzero elements, e.g., $A = G_{xxxx}$, $B = G_{xxyy}$, and $C = G_{xyxy}$. Therefore, the strain produces the perturbation of the form

$$\Delta D_{\alpha\beta} = G_{\alpha\beta\gamma\delta}u_{\gamma\delta} = \begin{pmatrix} Au_{xx} + Bu_{yy} & Cu_{xy} \\ Cu_{xy} & Bu_{xx} + Au_{yy} \end{pmatrix} \quad \text{(S7)}$$

Diagonalizing this matrix, we obtain Eq. (2) of the main text.

**Supplementary References**


S1. Hirth, J. P. and Lothe, J., Theory of dislocations (Krieger, Malabar, FL, 1982).

S2. Forwood, C. T. and Clarebrough, L. M., Hexagonal arrays of grain-boundary dislocations in coherent twin boundaries, Phil. Mag. Lett. A 53, L31-L34 (1985). DOI: https://doi.org/10.1080/01418618608242828

S3. Zhang, H., Zhang, C., Hu, T., Zhan, X., Wang, X., Zhou, Y., On the small angle twist sub-grain boundaries in $Ti_3AlC_2$, Sci. Rep. 6, 23943 (2016). DOI: https://doi.org/10.1038/srep23943

S4. Amelinckx, S. and Delavignette, P., Observation of dislocations in non-metallic layer structures, Nature 185, 603-604 (1960). DOI: https://doi.org/10.1038/185603a0

S5. Yamaguchi, H., Belk, J. G., Zhang, X. M., Sudijono, J. L., Fahy, M. R., Jones, T. S., Pashley, D. W., and Joyce, B. A., Atomic-scale imaging of strain relaxation via misfit dislocations in highly mismatched semiconductor heteroepitaxy: InAs/GaAs(111)A, Phys. Rev. B 55, 1337 (1997). DOI: https://doi.org/10.1103/PhysRevB.55.1337

S6. Chen, C., Wang, Z., Kato, T., Shibata, N., Taniguchi, T., and Ikuhara, Y., Misfit accommodation mechanism at the heterointerface between diamond and cubic boron nitride, Nature Comm. 6, 6327 (2015). DOI: https://doi.org/10.1038/ncomms7327

S7. Jiang, B.-Y. *et al.* Plasmon Reflections by Topological Electronic Boundaries in Bilayer Graphene, *Nano Lett*. **17**, 7080 (2017).

S8. Bosak, A., Serrano, J., Krisch, M., Watanabe, K., Taniguchi, T., and Kanda, H., Phys. Rev. B **73**, 041402(R) (2006). DOI: https://doi.org/10.1103/PhysRevB.73.041402

S9. Lebedev, A.V., Lebedeva, I.V., Knizhnik, A.A., Popov, A.M. Interlayer interaction and related properties of bilayer hexagonal boron nitride: ab initio study. *RSC Adv.* **6**, 6423 (2016).

S10. Yankowitz, M. et al. Pressure-induced commensurate stacking of graphene on boron nitride. Nature Comm. 7, 13168 (2016).

S11. Kim, K. et al. Tunable moiré bands and strong correlations in small-twist-angle bilayer graphene. PNAS, 114, 3364 (2017).

S12. Siems, R., Delavignette, P., and Amelinckx, S., The buckling of a thin plate due to the presence of an edge dislocation, Phys. Stat. Sol. (B) 2, 421-438 (1962). DOI: https://doi.org/10.1002/pssb.19620020407
S13. Butz, B., Dolle, C., Weber, F. N. D., Waldmann, D., Weber, H. B., Meyer, B., and Spiecker, E., Dislocations in bilayer graphene, Nature 505, 533 (2014). DOI: https://doi.org/10.1038/nature12780
S14. Weaire, D. and Hutzler, S. The Physics of Foams (Oxford University Press, Oxford, 1999).
S15. Fei, Z. *et al.* Infrared Nanoscopy of Dirac Plasmons at the Graphene-$SiO_2$ interface. *Nano Lett.* **11**, 4701-4705 (2011).
S16. Dai, S. *et al.* Tunable Phonon Polaritons in Atomically Thin van der Waals Crystals of Boron Nitride. *Science* **343**, 1125-1129, (2014).
S17. Caldwell, J. D. *et al*. Sub-diffractional, volume-confined polaritons in a natural hyperbolic material: hexagonal boron nitride. *Nature Commun*, **5**, 5221 (2014).
S18. Principi, A. *et al*. Plasmon losses due to electron-phonon scattering: the case of graphene encapsulated in hexagonal Boron Nitride. *Phys. Rev. B* **90**, 165408 (2014).
S19. Ni, G. X. et al. Fundamental limits to graphene plasmonics. *Nature* **557**, 530-533 (2018).